Available online at www.sciencedirect.com

jmr&t Journal of Materials Research and Technology

journal homepage: www.elsevier.com/locate/jmrt

Original Article

Effects of rolling reduction on Burgers orientation relationship and slip behavior of a Ti–5.5Mo–7.2Al–4.5Zr–2.6Sn–2.1Cr alloy

Duoduo Wang [a,b], *Qunbo Fan* [a,b,*], *Lin Yang* [a], *Haichao Gong* [a], *Jingjiu Yuan* [a], *Kai Chen* [a], *Xinjie Zhu* [a], *Xingwang Cheng* [a], *Zhiming Zhou* [c]

[a] *National Key Laboratory of Science and Technology on Materials Under Shock and Impact, School of Materials Science and Engineering, Beijing Institute of Technology, Beijing 100081, China*

[b] *Beijing Institute of Technology Chongqing Innovation Center, Chongqing 401135, China*

[c] *School of Materials Science and Engineering, Chongqing University of Technology, Chongqing 400054, China*

ARTICLE INFO

Article history:
Received 14 July 2021
Accepted 29 September 2021
Available online 1 October 2021

Keywords:
Titanium alloy
Hot rolling
Burgers orientation relationship
Schmid factor

ABSTRACT

The important but highly complex α/β Burgers orientation relationship and slip behavior of a Ti–5.5Mo–7.2Al–4.5Zr–2.6Sn–2.1Cr titanium alloy plate were obtained and elaborated, which was subjected to hot rolling with 20%, 40%, and 60% reductions in thickness. The electron backscatter diffraction statistical results showed that the Burgers orientation relationship was strictly maintained in the initial microstructure and exhibited a slight deviation of ~10° at 20% reduction. With the thickness reduction increasing to 40% and 60%, this classical relation between α- and β-Ti will be gradually broken. Furthermore, the low-angle grain boundaries fractions of the β phase were 94.95% and 92.77% at 20% and 40% reductions, respectively, indicating that the β phase had a significant contribution to the overall plastic deformation. For the α phase, the relative frequencies of the $<11\bar{2}0>\{0001\}\alpha$ and $<11\bar{2}0>\{10\bar{1}0\}\alpha$ slip systems were 32.81% and 44.43% at 20% reduction, respectively. Noticeably, under the applied loading of normal direction, the $<11\bar{2}0>\{0001\}\alpha$ slip system became more pronounced at 60% reduction (i.e., 59.01%) and, hence promoted a considerable strain partitioning in the α phase. In terms of typical α grains, an obvious intragranular misorientation diversity at 60% reduction was further traced, thereby reasonably leading to the Schmid factor gradient within grain interior and the breakdown of Burgers orientation relationship.

* Corresponding author.
E-mail address: fanqunbo@bit.edu.cn (Q. Fan).

https://doi.org/10.1016/j.jmrt.2021.09.135

1. Introduction

Hot rolling is a promising forming technique for titanium alloy components, which can enhance its service performance. Du et al. [1] revealed that rolling and solution treatment in the $\alpha + \beta$ field led to the better ductility than that in the β field. Chen et al. [2] investigated systematically the deformation behaviors of the hot-rolled Ti-55511 alloys under different reductions. It was found that the tensile strength and ductility can be improved with increasing the thickness reduction, which was attributed to the grain refinement and the fragment of grain boundary α phase. The service performance of titanium alloy is sensitive to the complex microstructural characteristics after hot rolling. Li et al. [3] studied the effect of rolling texture on the anisotropic tensile properties. Nasiri-Abarbekoh et al. [4] investigated the simultaneous effects of thickness and texture on mechanical properties anisotropy of commercially pure titanium. Zhang et al. [5] also confirmed that the inevitable rolling texture may cause the anisotropy of mechanical properties. Especially, Lei et al. [6] analyzed quantitatively the anisotropy mechanism along different loading directions, which was partly due to the existence of non-standard {0002} basal texture. Sahoo et al. [7] observed a dominant basal texture in hot-rolled commercially pure titanium samples regardless of the reduction percentages (50%, 70%, 80%, and 90% reductions). In addition, Warwick et al. [8] observed that the initial α (0002) texture in β-annealed Ti–6Al–4V alloy softened during rolling at 950 °C. In the β phase, Chen et al. [9] found that the weakening of texture components was accompanied by the occurrence of the dynamic recrystallization. Chen et al. [10] investigated the texture evolution in the Ti–15Mo–3Al–2.7Nb–0.2Si alloy during hot rolling at 1023 K. The electron backscatter diffraction (EBSD) analysis revealed that the formed dynamic recrystallization grains rotated towards the preferential slip systems with a rather large misorientation between them, thereby leading to the weakening of deformation texture.

In general, classical Burgers orientation relationship (BOR) will be maintained between α and the surrounding β grains, i.e., $(0001)_\alpha//(110)_\beta$, $<11\bar{2}0>_\alpha//<11\bar{1}>_\beta$ [11,12]. Leo Prakash et al. [13] characterized that most primary α grains strictly obeyed BOR with β phase despite the severe deformation of 77% reduction in thickness, and the α rolling texture was determined by the β phase as well as the variant selection. Obasi et al. [14] discussed the variant selection mechanism for special β grain pairs with common <110> poles, which was more prominent at the rolling temperature of 950 °C than 800 °C. Hence, in the material rolled at 950 °C, more α colonies with common <0002> poles on both sides of a former β grain boundary were observed. However, Gu et al. [15] suggested that the BOR will be broken down if the primary α precipitates and β matrix underwent simultaneously plastic deformation. Consequently, their deformation textures were significantly different. Obviously, to date, the previous studies are insufficient to reveal the orientation relationship evolution between α and β phases during hot rolling process.

Furthermore, the initial texture component and texture evolution can facilitate various slip modes in titanium alloy. The slip behavior associated with the α phase (hexagonal-close-packed, hcp) is particularly complicated, compared with the β phase with body-centered-cubic (bcc) crystalline structure. The main slip systems of the α phase are basal <a> slip ($<11\bar{2}0>\{0001\}$), prismatic <a> slip ($<11\bar{2}0>\{10\bar{1}0\}$), pyramidal <a> slip ($<11\bar{2}0>\{10\bar{1}1\}$), and pyramidal <c+a> slip ($<11\bar{2}3>\{10\bar{1}1\}$) [16]. Wang et al. [17] found that the initial $<11\bar{2}0>\{10\bar{1}0\}$ rolling texture resulted in the preferential activation of the pyramidal <c+a> slip. Nasiri-Abarbekoh et al. [18] studied the effect of strong basal texture on the activation of deformation systems when the rolling reduction reached to 50%. In addition, the compressive loading exerted at the normal direction (ND), rolling direction (RD), and transverse direction (TD) caused consequently their respective deformation mechanisms (e.g. basal <**a**> slip for the ND). Combining EBSD measurement and Schmid factor analysis, Won et al. [19] further explained that this deformation anisotropy was resulted from the specific rolling texture. Nevertheless, the slip behaviors of hot-rolled titanium alloys subjected to various thickness reductions have been scarcely reported.

Therefore, in this work, a Ti–5.5Mo–7.2Al–4.5Zr–2.6Sn–2.1Cr dual-phase alloy was hot rolled at 850 °C to 20%, 40%, and 60% reductions in thickness. The EBSD measurement was used to analyze the microstructural characteristics as well as the texture evolution. In particular, the coordinate deformation behavior of two phases (α and β) was discussed by tracking the BOR relations. Furthermore, the Schmid factor distributions of individual slip systems were thoroughly analyzed, thereby further revealing the slip behaviors of two phases.

2. Materials and methods

Prior to hot rolling, the titanium alloy (Ti–5.5Mo–7.2Al–4.5Zr–2.6Sn–2.1Cr) was forged and subsequently heat-treated (880 °C/0.5 h/FC + 740 °C/2 h/FC). A schematic of the hot rolling process is shown in Fig. 1. The β-transus temperature of this alloy was ~895 °C. Three specimens with dimension of 40 mm × 40 mm × 20 mm (RD × TD × ND) were cut and heated at 850 °C for 1 h in an air furnace. Afterward, the specimens were unidirectionally hot rolled in the $\alpha + \beta$ phase field to 20%, 40%, and 60% reductions in thickness (per pass: ~10%). The specimens will be reheated to the preset temperature for 2 min after two rolling passes. The rolling speed was 0.16 m/s. Consequently, the rolled sheets at the corresponding thickness of 14.4 mm, 10.8 mm, and 7.2 mm along the ND were obtained.

The EBSD measurement was used to characterize the microstructure and crystallographic orientation of the initial and hot-rolled specimens. To relieve residual stress, the surface layers were mechanically polished and electropolished in the electrolyte of 6% $HClO_4$, 34% $CH_3(CH_2)_3OH$, and 60% CH_3OH (30 s, accelerating voltage: 25 V). The EBSD scans on the RD-TD surface were performed on a HITACHI S-4800 N scanning electron microscope. The acceleration voltage and the step size were 20 kV and 0.5 μm, respectively. Subsequently, the collected data was processed with Oxford *HKL* Channel 5 software package.

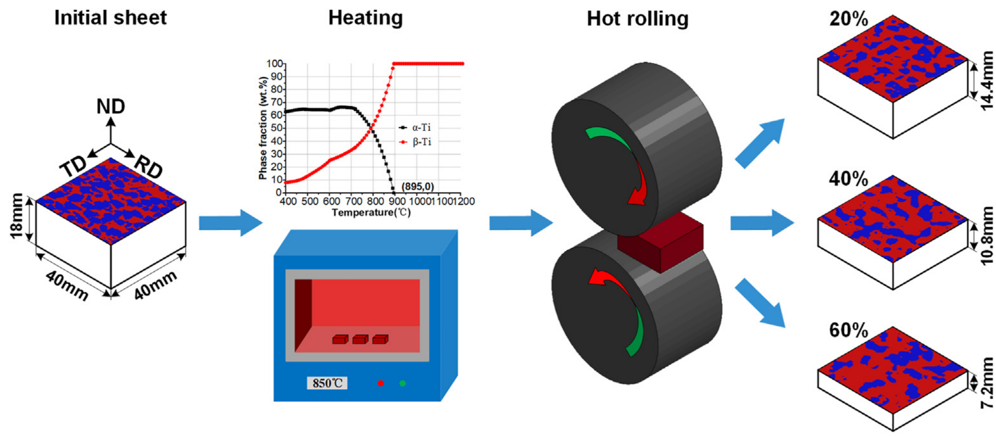

Fig. 1 – A schematic of the hot rolling process.

3. Results

3.1. Initial microstructure and crystallographic texture

Fig. 2 shows the initial microstructure and crystallographic texture of the Ti–5.5Mo–7.2Al–4.5Zr–2.6Sn–2.1Cr alloy via EBSD. Fig. 2(a) and (b) show the crystalline orientation maps of the α and β phases along the ND, respectively (comprising their histograms of grain size distribution, see the inset). The microstructure feature of equiaxial primary α phase and intergranular β matrix can be observed. The volume fraction of the α phase is 63.9% and that of 36.1% for the β phase. The considerable grain aggregates for the β phase exhibit similar crystallographic orientation, thus forming the macrozones [20]. The equivalent circle diameters of the α and β grains are 4.88 μm and 5.29 μm, respectively (see the corresponding inset). Fig. 2(c) show three representative pole figures for each phase, i.e., {0001}, {10$\bar{1}$0}, and {$\bar{1}$2$\bar{1}$0} for the α phase; {001}, {011}, and {111} for the β phase. The normal axis of the pole figures is the ND of the sheet. The initial alloy develops a main texture component that c-axes tilt ~40° from the ND towards the RD. Compared with the α phase, there is more random texture component in the β phase. Furthermore, the texture components in the {0001} or {$\bar{1}$2$\bar{1}$0} pole figure overlap with that in the {011} or {111} pole figure (see the rectangles or triangles with different colors), which indicates that the BOR

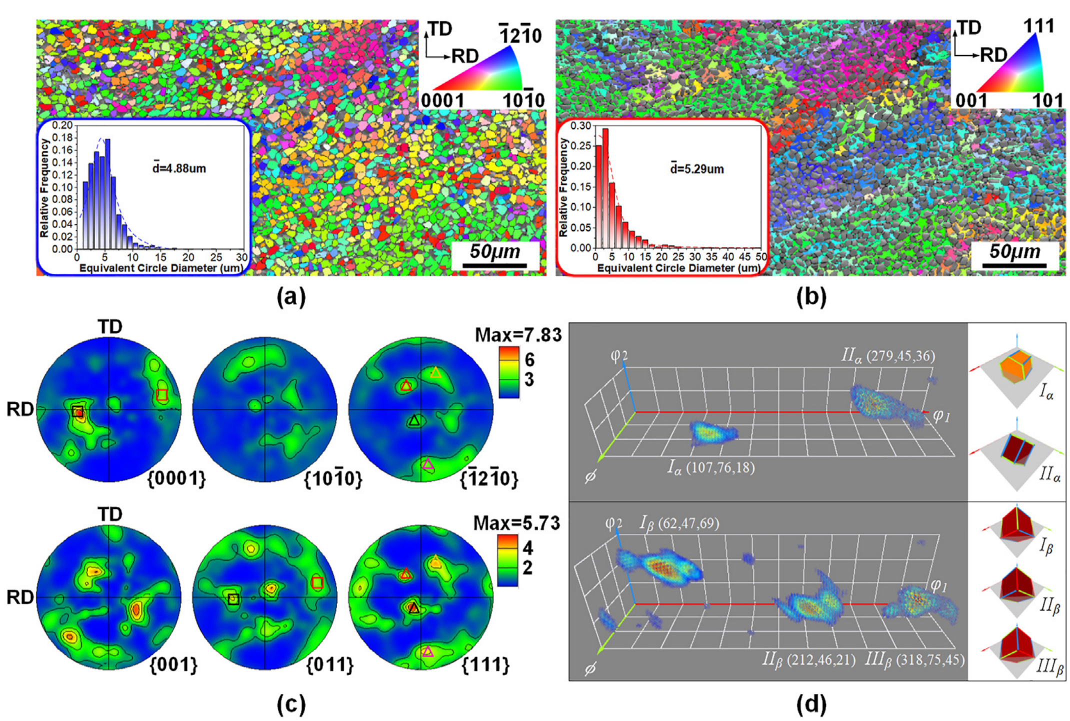

Fig. 2 – Initial microstructure and crystallographic texture: crystalline orientation maps of the α phase (a) and β phase (b), the corresponding texture pole figures and the 3D ODF distributions (c) and (d), respectively.

relation between the α grains and adjacent β matrix is always satisfied [21].

To further analyze intuitively the crystallographic orientation of each grain by the Euler angle (φ_1, φ, φ_2), Fig. 2(d) show the 3D orientation distribution function (ODF) distributions of the α and β phases. The Euler angle (φ_1, φ, φ_2) can be converted into the Miller index ($h\ k\ l$)<u v w>, according to the following expression [22]:

$$\begin{pmatrix} u & h \\ v & k \\ w & l \end{pmatrix} = \begin{bmatrix} \cos\varphi_1\cos\varphi_2 - \sin\varphi_1\sin\varphi_2\cos\varphi & \sin\varphi_2\sin\varphi \\ -\cos\varphi_1\sin\varphi_2 - \sin\varphi_1\cos\varphi_2\cos\varphi & \cos\varphi_2\sin\varphi \\ \sin\varphi_1\sin\varphi & \cos\varphi \end{bmatrix} \tag{1}$$

There are two main texture components of I_α(107, 76, 18) and II_α(279, 45, 36) in the α phase. For the β phase, the random spatial orientation distribution is pronounced in the Euler space, for instance, I_β(62, 47, 69), II_β(212, 46, 21), and III_β(318, 75, 45), which is consistent with analysis result of the pole figures (see Fig. 2(c)).

3.2. *Microstructure and texture evolution after hot rolling*

Fig. 3 shows the crystalline orientation maps along the ND and the hot-rolled pole figures for the α phase (i.e., {0001}, {10$\bar{1}$0}, and {$\bar{1}2\bar{1}$0}) at different thickness reductions. As shown in Fig. 3(a), the volume fraction of the α phase is 37.4% at 20% reduction. Compared with the initial microstructure (see Fig. 2(a)), the amount of α phase decreases significantly after hot rolling at 850 °C. This is consistent with the progressive decreasing tendency of α-Ti as the temperature increases from 720 °C to 895 °C (see the equilibrium phase diagram in Fig. 1). As shown in Fig. 3(b) and (c), when the rolling reduction reached to 40% and 60%, the volume fractions of the α phase are 35.4% and 36.9%, respectively. It can be concluded that the value of phase fraction is not sensitive to the rolling reduction. Furthermore, the histograms of grain size distribution with respect to the α grains are extracted from respective crystalline orientation maps (see the inset). The equivalent circle diameters relationship of the α grains at 20%, 40%, and 60% reductions can be described as follow: 2.66 μm > 2.31 μm > 1.99 μm, which implies the occurrence of grain refinement with increasing the thickness reduction. The significant refinement behavior of hot-rolled α grains can also be traced, compared with the value of 4.88 μm in the initial state (see Fig. 2(a)). In addition, at 20% reduction, the ND//<$\bar{1}2\bar{1}$0> is the dominant texture component with the maximum intensity of 4.97 Multiples of Uniform Density (MUD). Afterward, the α grains rotate towards favorable orientations under rolling load and, hence, the texture component with c-axes deviating ~20° from the ND is gradually formed at 40% reduction. This typical texture component is generally maintained but slightly

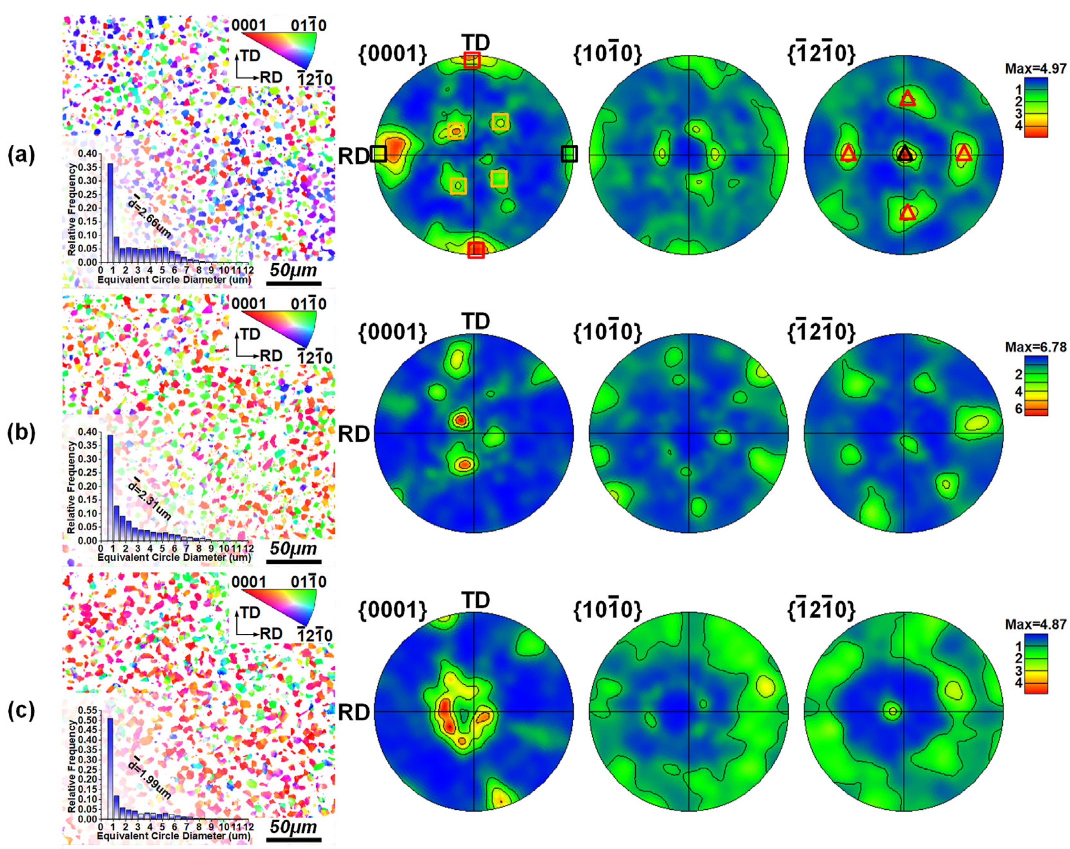

Fig. 3 – The crystalline orientation maps along the ND with the insets showing histograms of grain size distribution (left), and the {0001}, {10$\bar{1}$0}, and {$\bar{1}2\bar{1}$0} hot-rolled pole figures (right) for the α phase at different thickness reductions: (a) 20%, (b) 40%, and (c) 60%.

randomized at 60% reduction. Therefore, the texture-associated maximum intensity decreases from 6.78 MUD to 4.87 MUD.

Fig. 4 shows the crystalline orientation maps along the ND and the hot-rolled pole figures for the β phase (i.e., {001}, {101}, and {111}) at different thickness reductions. Complementary to the α phase (see Fig. 3), the volume fractions of the β phase at 20%, 40%, and 60% reductions are 62.6%, 64.6%, and 63.1%, respectively. Obviously, the phase fraction of the β phase is more sensitive to deformation temperature (initial state: 36.1%) than rolling reduction, as shown by the aforementioned result for the α phase in Fig. 3. The histograms of grain size distribution associated with the β grains are reproduced by the EBSD maps (see the inset). The equivalent circle diameters of the β phase at 20%, 40%, and 60% reductions are 2.88 μm, 2.66 μm, and 2.48 μm, respectively. The grain refinement behavior also exhibits high universality in the β phase. Through the comparison, it can be found that the mean diameter of the β grains is significantly larger than that of the α grains irrespective of initial and hot-rolled states. Furthermore, the ND//<001> texture component having the maximum intensity of 9.91 MUD is the strongest at 20% reduction. The existing texture components in the $\{0001\}_\alpha$ and $\{\bar{1}2\bar{1}0\}_\alpha$ pole figures, as shown by the rectangles and triangles in Fig. 3(a), are further labeled in the $\{011\}_\beta$ and $\{111\}_\beta$ pole figures (see Fig. 4(a)). The one-to-one positional relationship is not strictly maintained, indicating the deviation (~10°) of the BOR relation. Even at 40% reduction, more severe plastic deformation will lead to the breakdown of the BOR relation (see Figs. 3(b) and 4(b)). As shown in Figs. 3(c) and 4(c), this incoherent boundaries between α- and β-Ti are still prominent. The breakdown mechanism of the BOR relation will be further discussed in Section 4.2. In addition, the lattice reorienting response occurs in the β grains, thus gradually forming the ND//<111> texture component (6.65 MUD at 60% reduction).

A schematic of the lattice reorienting response at different thickness reductions is shown in Fig. 5. The volume fraction of the α phase (blue) decreases significantly after hot rolling and fluctuates slightly with the increase of thickness reduction. The equivalent circle diameters of the α grains and the surrounding β matrix (red) exhibit a decreasing tendency. The initial α texture with c-axes deviating ~40° from the ND towards the RD is replaced by the TD//<0001> and RD//<0001> transition textures at 20% reduction. Subsequently, the hot-rolled texture that c-axes align ~20° away from the ND dominates in the specimens with 40% and 60% reductions, while the orientation distribution of the latter is broader. Furthermore, the splitting of texture component is commonly observed in the β phase. Ultimately, the ND//<111> texture component is relatively pronounced after the ND//<001> transition texture (at 20% reduction).

To further reproduce the spatial distribution of orientation clustering in the Euler space, Fig. 6 shows the 3D ODF

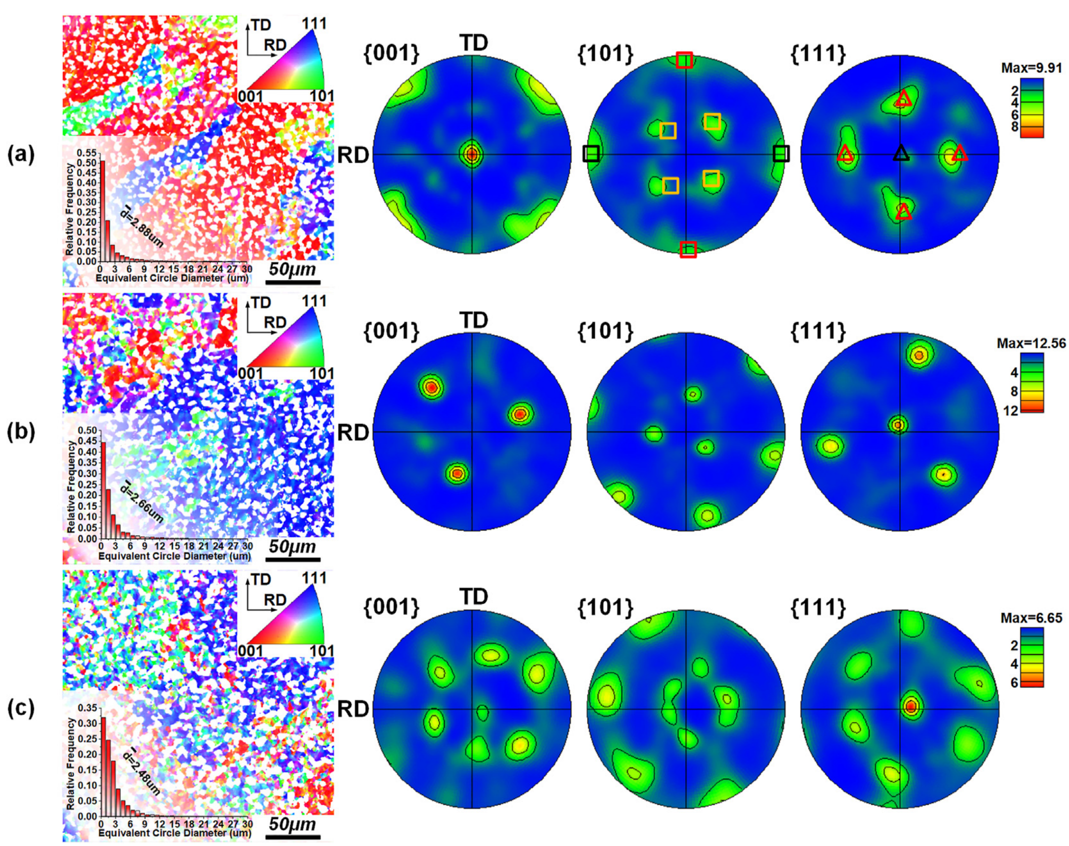

Fig. 4 – The crystalline orientation maps along the ND with the insets showing histograms of grain size distribution (left), and the {001}, {101}, and {111} hot-rolled pole figures (right) for the β phase at different thickness reductions: (a) 20%, (b) 40%, and (c) 60%.

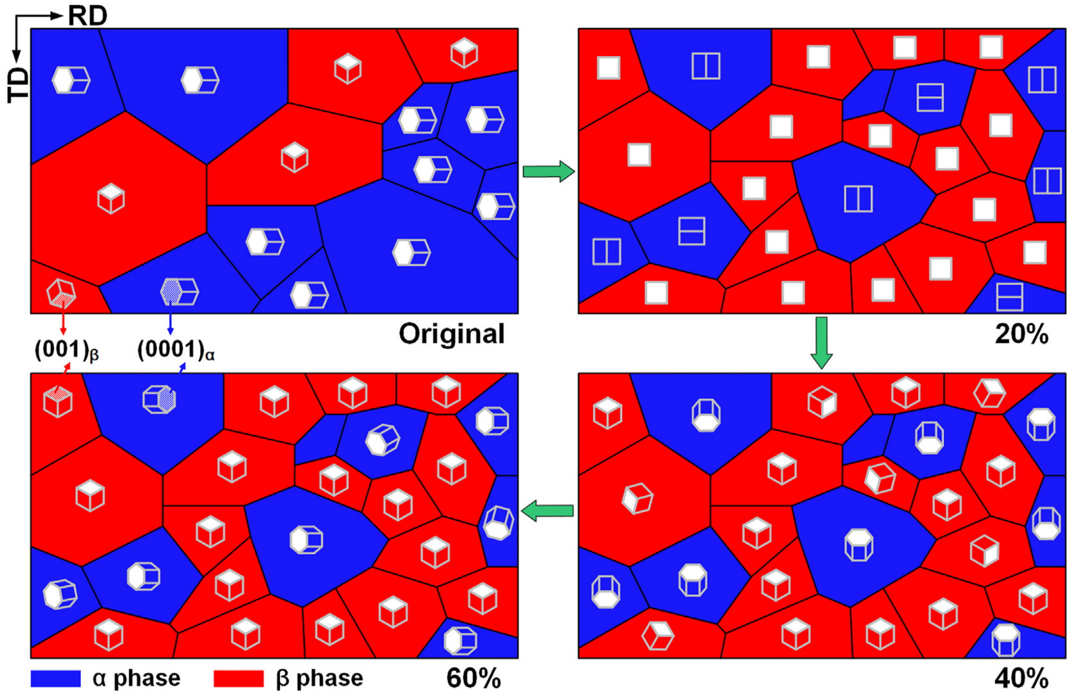

Fig. 5 – A schematic of the lattice reorienting response at different thickness reductions.

distributions at different thickness reductions. Fig. 6(a) shows the 3D ODF distributions of the α (left) and β (right) phases at 20% reduction. Considering the hexagonal crystal symmetry, the α phase exhibits three texture components: *20%-I*$_\alpha$(3, 87, 0), *20%-II*$_\alpha$(90, 79, 0), and *20%-III*$_\alpha$(181, 86, 0). Similarly, for the β phase, the main texture components, such as the *20%-I*$_\beta$(45, 87, 0), *20%-II*$_\beta$(137, 85, 0), *20%-III*$_\beta$(225, 86, 0), and *20%-IV*$_\beta$(315, 87, 0), can be ascertained. The unit cell models of individual representative textures, whose colors are associated with the unit triangle (the inverse pole figure), are fixed in a sample coordinate system. Fig. 6(b) and (c) show the 3D ODF distributions of the α (left) and β (right) phases at 40% and 60% reductions, respectively. At 40% reduction, the α texture is dominated by the *40%-I*$_\alpha$(40, 19, 0), whereas inhomogeneous distribution occurs in the β phase, i.e., *40%-I*$_\beta$(110, 54, 36), *40%-II*$_\beta$(223, 61, 45), and *40%-III*$_\beta$(338, 49, 54). This comparative assessment of two phases is also demonstrated in the hot-rolled microstructure of 60% reduction. There are the *60%-*

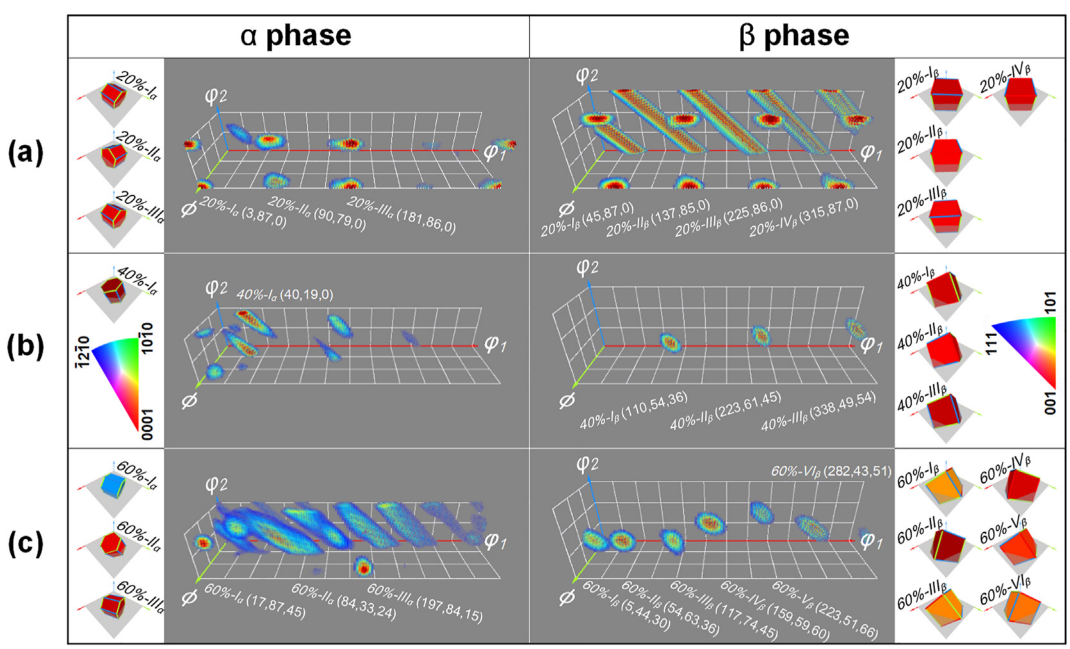

Fig. 6 – The 3D ODF distributions at different thickness reductions: (a) 20%, (b) 40%, and (c) 60%.

I_β(5, 44, 30), 60%-II_β(54, 63, 36), and 60%-III_β(117, 74, 45) texture components in the β phase, along with considerable contributions of the 60%-IV_β(159, 59, 60), 60%-V_β(223, 51, 66), and 60%-VI_β(282, 43, 51). The α phase, by contrast, has only three texture components of the 60%-I_α(17, 87, 45), 60%-II_α(84, 33, 24), and 60%-III_α(197, 84, 15). Furthermore, more severe rolling deformation of 60% reduction causes the orientation dispersion instead of traditional texture strengthening, which is in accordance with the lower values of maximum intensity in Figs. 3(c) and 4(c).

3.3. Misorientation distribution evolution after hot rolling

Fig. 7 shows the phase + grain boundaries maps as well as misorientation distribution histograms at different thickness reductions. The red and black lines in the phase + grain boundaries maps denote low-angle grain boundaries with <15° misorientation (LAGBs) and high-angle grain boundaries (>15° misorientation), respectively. The blue lines indicate the phase boundaries between α- and β-Ti. The grain boundaries density, especially the LAGBs (marked by the red lines), increases significantly with increasing the rolling reduction. Hu et al. [23] also confirmed that the alloys preserved an enormous number of LAGBs can readily accommodate plastic deformation by amplifying dislocation glide. In addition, the prominent LAGBs exists within β grain interior, while the nearly clear α grains are apparent, implying that the β phase has a considerable contribution to the rolling deformation, as reported in previous study [24]. As shown in Figs. 3 and 4, the volume fraction and equivalent circle diameter of the β phase are always greater than that of the α phase in hot-rolled microstructure. Therefore, the dislocation multiplication, local entanglement, and successive substructure boundaries are easier to be generated in the deformed β grains. Fig. 7(a) shows the misorientation distribution histograms of the α (center) and β (right) phases at 20% reduction. The fractions of LAGBs in the α and β phases are 71.27% and 94.95%, respectively. The higher value of the latter further quantitatively affirms that the β phase undergoes main plastic deformation. Fig. 7(b) and (c) show the misorientation distribution histograms of the α (center) and β (right) phases at 40% and 60% reductions, respectively. The fraction of LAGBs in the α phase progressively increases and reaches a maximum value of 89.89% at 60% reduction. The β phase has an inverse decreasing tendency (minimum: 86.57%), even lower than the corresponding value of the α phase at 60% reduction. Germain et al. [25] revealed that this phenomenon may be attributed to the preferential recrystallization behavior of the β grains.

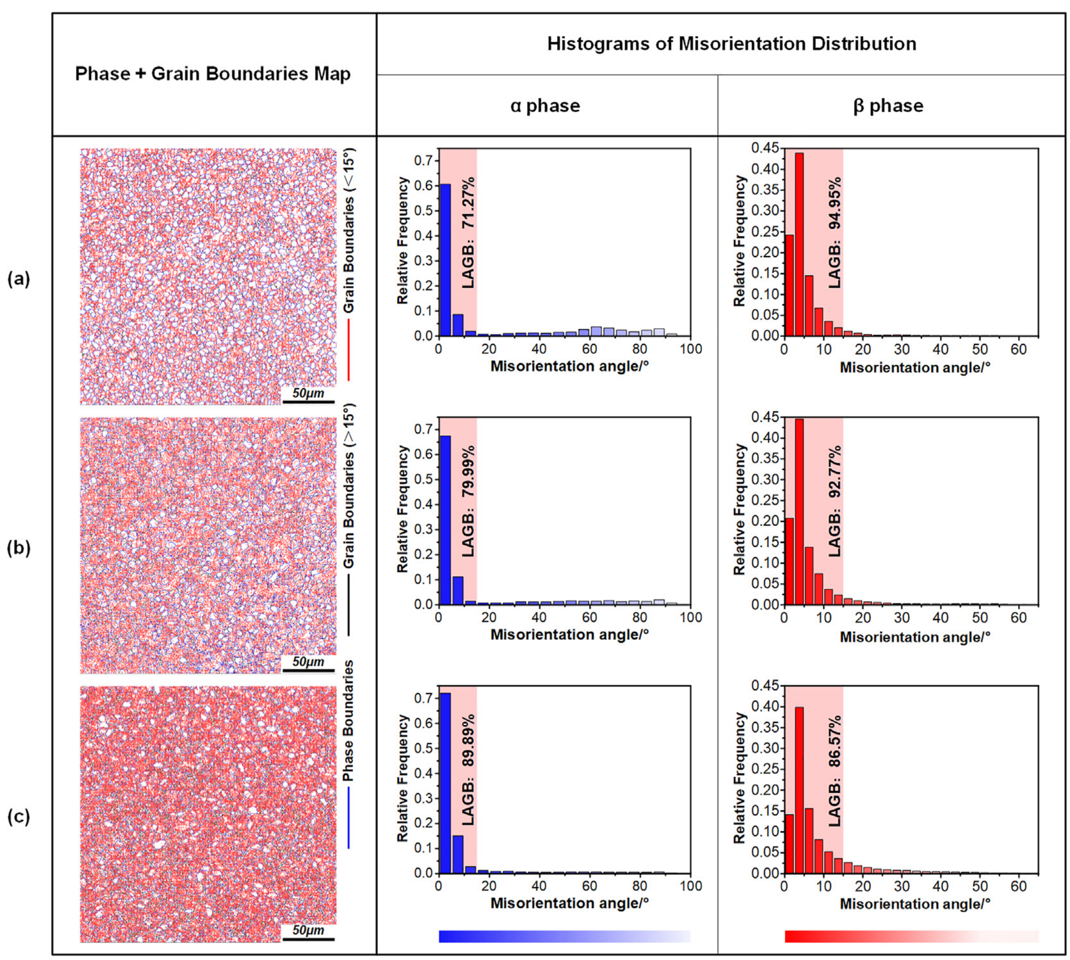

Fig. 7 – Phase + grain boundaries maps as well as misorientation distribution histograms at different thickness reductions: (a) 20%, (b) 40%, and (c) 60%.

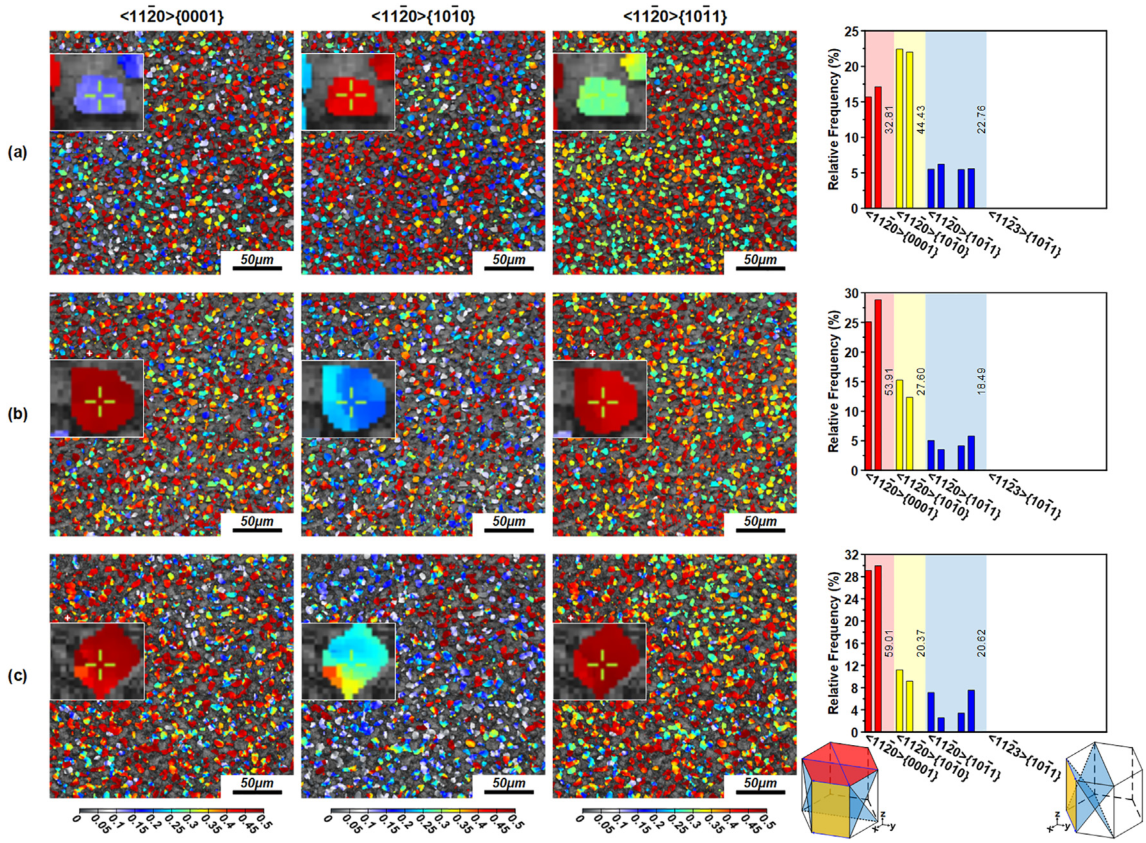

Fig. 8 – Schmid factor maps and frequency histograms of the $<11\bar{2}0>\{0001\}$, $<11\bar{2}0>\{10\bar{1}0\}$, and $<11\bar{2}0>\{10\bar{1}1\}$ slip systems along the ND for the α phase at different thickness reductions: (a) 20%, (b) 40%, and (c) 60%.

4. Discussion

4.1. *Schmid factor and relative frequency of slip systems after hot rolling*

Fig. 8 shows the Schmid factor maps and frequency histograms of slip systems along the ND for the α phase at different thickness reductions. The Schmid factor of the pyramidal <c+a> slip, i.e., $<11\bar{2}3>\{10\bar{1}1\}$ slip system, remains zero at various thickness reductions, so it can be reasonably ignored in the following discussion. Fig. 7(a) shows the Schmid factor maps and frequency histograms of the $<11\bar{2}0>\{0001\}$, $<11\bar{2}0>\{10\bar{1}0\}$, and $<11\bar{2}0>\{10\bar{1}1\}$ <a> slip systems at 20% reduction. The grains are color-coded as a function of the Schmid factor, and red and blue represent the maximum and minimum values (0.5 and 0) respectively. The Schmid factor of the $<11\bar{2}0>\{0001\}$ slip system is slightly lower than that of the $<11\bar{2}0>\{10\bar{1}0\}$ slip system.

The relative frequency of each slip system V^ican be calculated according to the following equation:

$$V^i = \gamma^i \Big/ \sum_{j=1}^{N} \gamma_j^i \tag{2}$$

where γ^irepresent the activated number of the slip system *i*. *N* is number of available slip systems, which is 3 for the α phase in this work.

Therefore, the relative frequencies of the $<11\bar{2}0>\{0001\}$ and $<11\bar{2}0>\{10\bar{1}0\}$ slip systems are 32.81% and 44.43% at 20% reduction, respectively. Fig. 7(b) and (c) show the Schmid factor maps and frequency histograms of the $<11\bar{2}0>\{0001\}$, $<11\bar{2}0>\{10\bar{1}0\}$, and $<11\bar{2}0>\{10\bar{1}1\}$ <a> slip systems at 40% and 60% reductions, respectively. Statistically, at 40% and 60% reductions, the plastic contributions of the $<11\bar{2}0>\{0001\}$ slip system are 53.91% and 59.01%, respectively, which are greater than those of the $<11\bar{2}0>\{10\bar{1}0\}$ slip system (corresponding value: 27.60% and 20.37%). Meanwhile, under the premise of ND loading condition, the α grains will be reoriented towards the favorable orientation for activating $<11\bar{2}0>\{0001\}$ slip system, while the Schmid factor of the $<11\bar{2}0>\{10\bar{1}0\}$ slip system decreases significantly (see the Schmid factor maps). Zaefferer [26] has demonstrated that basal slip had a lower critical resolved shear stress than prismatic slip. Therefore, the $<11\bar{2}0>\{0001\}$ slip system has the lowest critical resolved shear stress and higher Schmid factor, thereby promoting its significant strain partitioning in the α phase. For the $<11\bar{2}0>\{10\bar{1}1\}$ slip system, the relative frequencies of 20%, 40%, and 60% reductions are 22.76%, 18.49%, and 20.62%, respectively. The dislocation movement along the $<11\bar{2}0>\{10\bar{1}1\}$ slip system is strongly impeded owing to the higher critical resolved shear stress, even at the higher Schmid factor. Furthermore, the insets show the magnified Schmid factor maps of typical grains. The intragranular non-uniform distribution of the

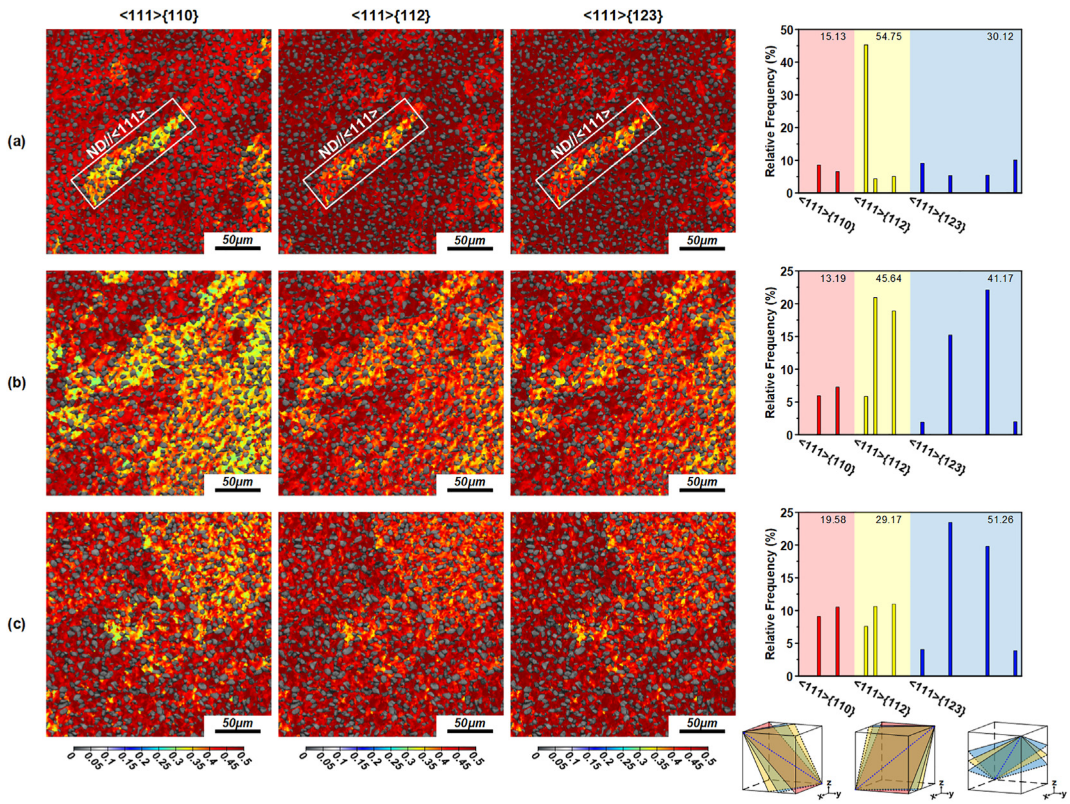

Fig. 9 – Schmid factor maps and frequency histograms of the <111>{110}, <111>{112}, and <111>{123} slip systems along the ND for the β phase at different thickness reductions: (a) 20%, (b) 40%, and (c) 60%.

Schmid factor becomes pronounced with increasing the thickness reduction, and a more detailed discussion will be given in section 4.2.

Fig. 9 shows the Schmid factor maps and frequency histograms of the <111>{110}, <111>{112}, and <111>{123} slip systems along the ND for the β phase at different thickness reductions. The Schmid factors are always at a higher level among all slip systems, which is independent of rolling reduction. In particular, the Schmid factors of each slip system in several macrozones with ND//<111> orientation (e.g. the white solid rectangles in Fig. 9(a)) are relatively lower than that in other regions.

It is generally known that the Schmid factor of the slip system *i* can be given as follow:

$$SF^i = \cos\lambda \cos\delta \tag{3}$$

where λ is the angle between loading direction and slip direction; δ is the angle between loading direction and the normal direction of slip plane.

In essence, these special grains having ND//<111> orientation satisfy the angle relationship $\delta \approx 90°$ and, hence, lower Schmid factor occurs in local deformation zones. Furthermore, the relative frequency of the <111>{112} slip system decreases monotonically from 54.75% at 20% reduction, while the <111>{123} slip system shows an opposite tendency (20% reduction: 30.12%). At 60% reduction, the relative frequencies of the <111>{110}, <111>{112}, and <111>{123} slip systems are 19.58%, 29.17%, and 51.26%, respectively. The four considered slip families of the <111>{123} slip system make significant contribution to the plastic deformation of the β phase.

4.2. *Intragranular misorientation of hot-rolled α grains*

To further analyze the heterogeneous distribution of the intragranular Schmid factor in Fig. 8, Fig. 10 shows the local orientation of three typical α grains at different thickness reductions. The existing colors are dependent on the Euler angle sites in the unit triangle. Fig. 10(a) shows the crystalline orientation map along the ND and the corresponding {0001} pole figure of a α grain at 20% reduction. The substantially uniform Euler angle of (171.4, 82.5, 30.6) and a unique orientation-associated position in {0001} pole figure can be observed, indicating the limited localized grain rotation. As shown in Fig. 10(b), when rolling reduction increases to 40%, a new orientation (60, 137.6, 49.3) in a special α grain with an initial Euler angle of (53.3, 139.9, 39.9) appears gradually (see the bottom left-hand corner). This intragranular misorientation gradient results in a slight deviation of ~5° in {0001} pole figure. Fig. 10(c) shows the crystalline orientation map along the ND and the corresponding {0001} pole figure of a special α grain with an initial Euler angle of (32.8, 44, 73) at 60% reduction. The localized distribution diversity of intragranular orientation is very noticeable under more severe deformation condition. As a result, three new orientations of (29.5, 55.8,

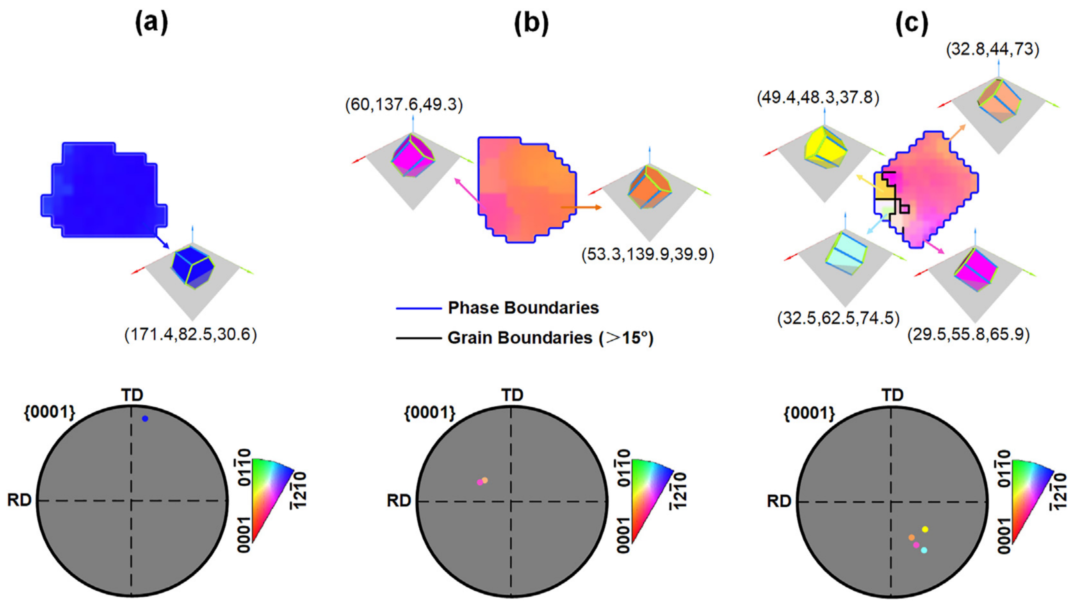

Fig. 10 – Intergranular orientation of three typical α grains at different thickness reductions: (a) 20%, (b) 40%, and (c) 60%.

65.9), (49.4, 48.3, 37.8), and (32.5, 62.5, 74.5) are expressed precisely, thus facilitating the significant difference (~30°) among directions in {0001} pole figure. The accumulated intragranular misorientation satisfies the high-angle grain boundaries criterion (>15° misorientation, marked by the black lines), and the microstructural characteristics of continuous dynamic recrystallization is visualized, as also reported in the literature [27]. Chen et al. [28] found that the formation of recrystallized grains resulted in a large deviation of the BOR after 80% rolling reduction. Therefore, the one-to-one positional relationship between α- and β-Ti, i.e., BOR relation, will be easily broken down (see Figs. 3 and 4) due to the continuous dynamic recrystallization behavior. On the other hand, the intragranular misorientation, based on the stress anisotropy caused by severe deformation, becomes more and more significant, which leads to the heterogeneous distribution of the Schmid factor.

5. Conclusions

In this work, a Ti–5.5Mo–7.2Al–4.5Zr–2.6Sn–2.1Cr titanium alloy was hot rolled to 20%, 40%, and 60% reductions in thickness at 850 °C. The complex BOR relations and slip behaviors were systematically investigated via EBSD measurement. The main conclusions can be drawn as follows:

(1) The classical BOR relation is strictly maintained in the initial microstructure and a slight deviation of ~10° can be observed at 20% reduction. Subsequently, this relationship between α- and β-Ti will be gradually broken when the thickness reduction reaches to 40% and 60%.
(2) A higher LAGBs density, volume fraction (at 40% reduction: 92.77% and 64.6%, respectively), and a higher equivalent circle diameter can be commonly observed within hot-rolled β grains, implying that the prominent strain partitioning takes place in the β phase. Furthermore, when the rolled sheet is loaded along the ND, the <11$\bar{2}$0>{10$\bar{1}$0}α slip system is relatively pronounced at 20% reduction (i.e., 44.43%). Under more severe deformation, the α grains will rotate towards the favorable orientation for activating <11$\bar{2}$0>{0001}α slip system, thereby leading to the higher relative frequency of 59.01% at 60% reduction.
(3) At 60% reduction, there is an obvious intragranular misorientation diversity, which can reasonably cause the Schmid factor gradient.

Declaration of Competing Interest

The authors declare that they have no known competing financial interests or personal relationships that could have appeared to influence the work reported in this paper.

Acknowledgments

This work was financially supported by the Natural Science Foundation of Chongqing (Grant No. Cstc2020jcyj-msxmX0094), and the Joint Research Programs between Belarusian Republican Foundation for Fundamental Research and Beijing Institute of Technology “BRFFR-BIT-2020” (Grant No. BITBLR2020004). Dr. Zheng from ZKKF (Beijing) Science & Technology Co., Ltd is acknowledged for EBSD tests. Analysis Tools for Electron and X-ray diffraction, ATEX – software, powered by B. Beausir and J.-J. Fundenberger, is acknowledged for assistance in EBSD analysis.

REFERENCES

[1] Du ZX, Xiao SL, Shen YP, Liu JS, Liu J, Xu LJ, et al. Effect of hot rolling and heat treatment on microstructure and tensile properties of high strength beta titanium alloy sheets. Mater Sci Eng A 2015;631:67–74.

[2] Chen W, Li C, Zhang XY, Chen C, Lin YC, Zhou KC. Deformation-induced variations in microstructure evolution and mechanical properties of bi-modal Ti-55511 titanium alloy. J Alloy Compd 2019;783:709–17.

[3] Li WY, Chen ZY, Liu JR, Zhu SX, Sui GX, Wang QJ. Rolling texture and its effect on tensile property of a near-α titanium alloy Ti60 plate. J Mater Sci Technol 2019;35:790–8.

[4] Nasiri-Abarbekoh H, Ekrami A, Ziaei-Moayyed AA. Effects of thickness and texture on mechanical properties anisotropy of commercially pure titanium thin sheets. Mater Des 2013;44:528–34.

[5] Zhang ZX, Fan JK, Li RF, Kou HC, Chen ZY, Wang QJ, et al. Orientation dependent behavior of tensile-creep deformation of hot rolled Ti65 titanium alloy sheet. J Mater Sci Technol 2021;75:265–75.

[6] Lei ZN, Gao PF, Wang XX, Zhan M, Li HW. Analysis of anisotropy mechanism in the mechanical property of titanium alloy tube formed through hot flow forming. J Mater Sci Technol 2021;86:77–90.

[7] Sahoo SK, Sabat RK, Sahni S, Suwas S. Texture and microstructure evolution of commercially pure titanium during hot rolling: role of strain-paths. Mater Des 2016;91:58–71.

[8] Warwick JLW, Jones NG, Bantounas I, Preuss M, Dye D. In situ observation of texture and microstructure evolution during rolling and globularization of Ti–6Al–4V. Acta Mater 2013;61:1603–15.

[9] Chen JH, Li JS, Tang B, Chen Y, Kou HC. Microstructure and texture evolution of a near β titanium alloy Ti-7333 during continuous cooling hot deformation. Prog Nat Sci 2019;29:50–6.

[10] Chen Y, Li JS, Tang B, Kou HC, Xue XY, Cui YW. Texture evolution and dynamic recrystallization in a beta titanium alloy during hot-rolling process. J Alloy Compd 2015;618:146–52.

[11] Shi R, Dixit V, Viswanathan GB, Fraser HL, Wang Y. Experimental assessment of variant selection rules for grain boundary α in titanium alloys. Acta Mater 2016;102:197–211.

[12] Zhao ZB, Wang QJ, Liu JR, Yang R. Effect of heat treatment on the crystallographic orientation evolution in a near-α titanium alloy Ti60. Acta Mater 2017;131:305–14.

[13] Leo Prakash DG, Honniball P, Rugg D, Withers PJ, Quinta da Fonseca J, Preuss M. The effect of β phase on microstructure and texture evolution during thermomechanical processing of α + β Ti alloy. Acta Mater 2013;61:3200–13.

[14] Obasi GC, Birosca S, Leo Prakash DG, Quinta da Fonseca J, Preuss M. The influence of rolling temperature on texture evolution and variant selection during α → β → α phase transformation in Ti–6Al–4V. Acta Mater 2012;60:6013–24.

[15] Gu B, Chekhonin P, Schaarschuch R, Oertel C-G, Xin SW, Ma CL, et al. Microstructure, texture and hardness of a metastable β-titanium alloy after bar-rolling and annealing. J Alloy Compd 2020;825:154082.

[16] Cizek P, Kada SR, Wang JT, Armstrong N, Antoniou RA, Lynch PA. Dislocation structures representing individual slip systems within the α phase of a Ti–6Al–4V alloy deformed in tension. Mater Sci Eng A 2020;797:140225.

[17] Wang CL, Yu DP, Niu ZQ, Zhou WL, Chen GQ, Li ZQ, et al. The role of pyramidal <c + a> dislocations in the grain refinement mechanism in Ti-6Al-4V alloy processed by severe plastic deformation. Acta Mater 2020;200:101–15.

[18] Nasiri-Abarbekoh H, Ekrami A, Ziaei-Moayyed AA, Shohani M. Effects of rolling reduction on mechanical properties anisotropy of commercially pure titanium. Mater Des 2012;34:268–74.

[19] Won JW, Park CH, Hong SG, Lee CS. Deformation anisotropy and associated mechanisms in rolling textured high purity titanium. J Alloy Compd 2015;651:245–54.

[20] Bantounas I, Dye D, Lindley TC. The role of microtexture on the faceted fracture morphology in Ti–6Al–4V subjected to high-cycle fatigue. Acta Mater 2010;58:3908–18.

[21] Wang DD, Fan QB, Shi R, Zhou Y, Gong HC, Wang L, et al. In-situ investigation via high energy X-ray diffraction of stress-induced $(0002)_{\alpha} \rightarrow (110)_{\beta}$ transformation in a Ti-5.5Mo-7.2Al-4.5Zr-2.6Sn-2.1Cr alloy. Mater Sci Eng A 2020;779:139154.

[22] Wu C, Huang L, Li CM. Experimental investigation on dynamic phase transformation and texture evolution of Ti55531 high strength titanium alloy during hot compression in the α+β region. Mater Sci Eng A 2020;773:138851.

[23] Hu T, Ma K, Topping TD, Saller B, Yousefiani A, Schoenung JM, et al. Improving the tensile ductility and uniform elongation of high-strength ultrafine-grained Al alloys by lowering the grain boundary misorientation angle. Scr Mater 2014;78–79:25–8.

[24] Wang K, Wu MY, Yan ZB, Li DR, Xin RL, Liu Q. Microstructure evolution and static recrystallization during hot rolling and annealing of an equiaxed-structure TC21 titanium alloy. J Alloy Compd 2018;752:14–22.

[25] Germain L, Gey N, Humbert M, Bocher P, Jahazi M. Analysis of sharp microtexture heterogeneities in a bimodal IMI 834 billet. Acta Mater 2005;13:3535–43.

[26] Zaefferer S. A study of active deformation systems in titanium alloys: dependence on alloy composition and correlation with deformation texture. Mater Sci Eng A 2003;344:20–30.

[27] Dong RF, Li JS, Kou HC, Tang B, Hua K, Liu SB. Characteristics of a hot-rolled near β titanium alloy Ti-7333. Mater Charact 2017;129:135–42.

[28] Chen W, Wang HD, Lin YC, Zhang XY, Chen C, Lv YP, et al. The dynamic responses of lamellar and equiaxed near β-Ti alloys subjected to multi-pass cross rolling. J Mater Sci Technol 2020;43:220–9.